Chemical Engineering Journal 144 (2008) 277–288

Contents lists available at ScienceDirect

Chemical Engineering Journal

journal homepage: www.elsevier.com/locate/cej

CFD simulation of bubbly two-phase flow in horizontal pipes

K. Ekambara, R.S. Sanders, K. Nandakumar*, J.H. Masliyah

Department of Chemical and Materials Engineering, University of Alberta, Edmonton, AB, Canada T6G 2G6

ARTICLE INFO

Article history:
Received 29 June 2007
Received in revised form 23 March 2008
Accepted 6 June 2008

Keywords:
Two-phase flows
CFD
Population balance
Flow pattern
Horizontal pipes

ABSTRACT

The internal phase distribution of co-current, air-water bubbly flow in a 50.3 mm i.d. horizontal pipeline has been modeled using the volume averaged multiphase flow equations. Liquid and gas volumetric superficial velocities varied in the range from 3.8 to 5.1 m/s and 0.2–1.0 m/s, respectively, and average gas volume fraction varied in the range from 4 to 16%. The predicted gas volume fraction and the mean liquid velocity are compared with the experimental data of Kocamustafaogullari and Wang [G. Kocamustafaogullari, Z. Wang, An experimental study on local interfacial parameters in a horizontal bubbly two-phase flow, Int. J. Multiphase Flow 17 (1991) 553–572], Kocamustafaogullari and Huang [G. Kocamustafaogullari, W.D. Huang, Internal structure and interfacial velocity development for bubbly two-phase flow, Nucl. Eng. Des. 151 (1994) 79–101] and Iskandrani and Kojasoy [A. Iskandrani, G. Kojasoy, Local void fraction and velocity field description in horizontal bubbly flow, Nucl. Eng. Des. 204 (2001) 117–128]. Good quantitative agreement with the experimental data is obtained with two different models (i.e., k–ε with constant bubble size and k–ε with population balance model). The model prediction shows better agreement with the experimental data with population balance than the constant bubble size predictions. The results indicate that the volume fraction has a maximum near the upper pipe wall, and the profiles tend to flatten with increasing liquid flow rate. It was found that increasing the gas flow rate at fixed liquid flow rate would increase the local volume fraction. The axial liquid mean velocity showed a relatively uniform distribution except near the upper pipe wall. An interesting feature of the liquid velocity distribution is that it tends to form a fully developed turbulent pipe-flow profile at the lower part of the pipe irrespective of the liquid and gas superficial velocities.

1. Introduction

Bubbly flows are of great importance in the chemical and process industries. A number of contacting devices operate under bubbly flow conditions in order to attain large interfacial areas for heat and mass transfer. The bubbly two-phase flow pattern is characterized by the presence of bubbles dispersed in a continuous liquid phase, with their maximum size being much smaller than the diameter of the containing vessel or pipe.

Horizontal flows have received less attention in the literature than vertical flows, even though this flow orientation is common in the industrial application such as hydrotransport, an important technology in bitumen extraction. Experimental observations are also difficult in this case, as the migration of dispersed bubbles towards the top of the pipe, due to buoyancy, causes a highly non-symmetric volume fraction distribution in the pipe cross-section. This density stratification is often accompanied by a strong secondary flow. In the literature, several measurement techniques have been used to describe the flow pattern in vertical [1–9] and horizontal pipe flows [10–13]. The difficulties in obtaining similar experimental results or convergent analysis undoubtedly stems from our lack of understanding of the mechanisms involved in determining the internal structure of bubbly two-phase flow. The influence of entrance effects is not fully understood either. The problems of characterizing the phase distributions by detailed measurement are further complicated by the fact that pipeline flows of gas-liquid mixtures need not always exhibit a fully developed equilibrium condition. Under certain conditions there may be periodic wavy flow in the axial directions. The expansion of the gas phase associated with the frictional pressure gradient also causes a continuous acceleration of the mixture, and, consequently, a continuous flow development in the axial direction. There are no theoretical models or fundamental studies available on the local distribution of gas volume fraction, liquid velocity and turbulence field in horizontal two-phase pipe flows.

In view of the current status on this subject, it is desirable to undertake a systematic investigation of the internal flow structure and flow field of two-phase flow in horizontal pipes and to develop a

* Corresponding author. Tel.: +1 780 492 5810; fax: +1 780 492 2881.
E-mail address: kumar.nandakumar@ualberta.ca (K. Nandakumar).

1385-8947/$ – see front matter © 2008 Elsevier B.V. All rights reserved.
doi:10.1016/j.cej.2008.06.008

Nomenclature

C_μ, $C_{\varepsilon1}$, $C_{\varepsilon2}$	constants in k–ε model
C_1, C_2	constants is used in Eq. (8)
C_D	drag coefficient
C_L	lift coefficient
C_{TD}	turbulent dispersion coefficient
d_b	bubble diameter (m)
g	gravity acceleration (m/s^2)
G	turbulence production term (J/m^3 s)
k	turbulent kinetic energy (m^2/s^2)
$\dot{m}$	mass flux per control volume (kg/m^3 s)
M	interphase transfer term (N/m^3)
n_w	unit normal pointing away from the wall
N_P	number of phase
p	pressure (N/m^2)
r, R	radius of the pipe (m)
Re	particle Reynolds number, $Re = d_b\|\mathbf{u}_r\|/\nu_c$
S	source term, *various*
t	time (s)
u	velocity vector (m/s)
$\mathbf{u}_r$	slip velocity (m/s)
V_G	volumetric superficial gas velocity (m/s)
V_L	volumetric superficial liquid velocity (m/s)
x	spatial coordinates (m)
y_w	distance to the nearest wall (m)

Greek letters

ϕ	transport variable
ρ	density (kg/m^3)
ε	turbulent dissipation rate (m^2/s^3)
μ	viscosity (kg/m s)
σ_k, σ_ε	constants in k–ε model
ν	kinematic viscosity (m^2/s)

Subscripts

α, β	phases
b	bubble
c, d	continuous, disperse
i, j	spatial directions
g, l	gas, liquid
lam, tur	laminar, turbulent
eff	effective

Superscripts

D	drag
L	lift
LUB	lubricant
TD	turbulent dispersion
VM	virtual

comprehensive computational fluid dynamics (CFD) model for prediction of the same. Further, simulations have been carried out to investigate the effect of volumetric superficial liquid and gas velocities on flow fields. The model (k–ε model with constant bubble size of 2 mm and k–ε with population balance model) predictions were compared with the experimental data available in the literature. CFD models, when carefully explored and matched with detailed experimental data, provide another means of exploring the relative importance of various mechanisms such as drag, lift forces on the observed spatial distributions of flow profiles. While studies on single particles/bubbles attest to the presence of such mechanisms in a precise quantitative manner, volume averaged models used for studying multiphase flows require the determination of closure relationships for such mechanisms in an empirical manner and CFD models together with careful experimental data provide a means of developing such closure models and exploring the consequences and sensitivities of such models on the predicted flow fields.

2. Definitions of flow patterns for gas–liquid two-phase flow in horizontal pipes

A flow pattern represents the state in which a multiphase flow appears under a given operating conditions in a certain device. For gas–liquid two-phase flow in horizontal pipes, Govier and Aziz [14] presented a detailed description of all possible flow patterns relevant to operating conditions such as superficial gas and liquid velocities. Based on the classification of a phase as being dispersed or continuous, full range of flow patterns can be classified into five groups, namely bubble flow, plug flow, slug flow, wave flow and annular flow, as shown in Fig. 1. Most researchers focus on bubble flow which can exist over a wide range of operating conditions. There is little agreement as to the definition of bubble flow. Bubble flow is divided into several sub-flow patterns by some authors, for example, dispersed bubble flow and elongated bubble flow [15] or dispersed bubble flow and bubble flow [16].

In the present work the notion of the dominant mechanism [17] is adopted to define the full range of flow patterns for gas–liquid two-phase flow in horizontal pipes. If gas flow rate is increasing gradually with a constant liquid flow rate, or vice versa, three dominant conditions appear alternatively between the gas phase and the liquid phase. The three dominant conditions are known as gas dominant, gas–liquid coordinated and liquid dominated. In the gas dominant regime, liquid exists in droplets and its movement is controlled by the gas phase, for instance, mist flow. In the liquid dominant regime, gas bubbles form and their movement is controlled by the liquid phase: for example, dispersed bubble flow. In gas–liquid coordinated regime, neither of the gas phase nor the liquid phase can dominate the other one: examples include buoyant bubble flow, slug flow and wave flow.

Of all the above mentioned flow regimes, dispersed bubble flow and buoyant bubble flow are of greatest interest because of their capability to provide large interfacial areas for heat and mass transfer in general and for attachment to bitumen in particular in hydrotransport. The commonality of the two regimes is the existence of bubbles. Therefore sometimes they are called bubble flow without discrimination. In fact there is a big difference between dispersed bubble flow and buoyant bubble flow: namely, the role of buoyancy. In dispersed bubble flow the buoyancy can be neglected compared with the effect of the liquid action on the gas phase. In dispersed flow, the bubbles move in horizontal pipes with some symmetry about the pipe axis. In the buoyant bubble flow regime, though, buoyancy plays an important role and the concentration of bubbles in this regime is asymmetrical about the pipe axis. Through the effect of buoyancy, bubbles are observed to move from the pipe bottom to the pipe top. The buoyant flow regime is widely investigated by many researchers: for example, Holmes and Russell [18]; Kocamustafaogullari and Huang [12]; Beattie [19]; Andreussi et al. [15]; and Iskandrani and Kojasoy [13]. It is this regime that is of interest to us.

3. Mathematical modeling

The objective of this study is to get the complete information on the three dimensional flow fields in terms of volume averaged velocities and volume fraction. The mean fields are of course

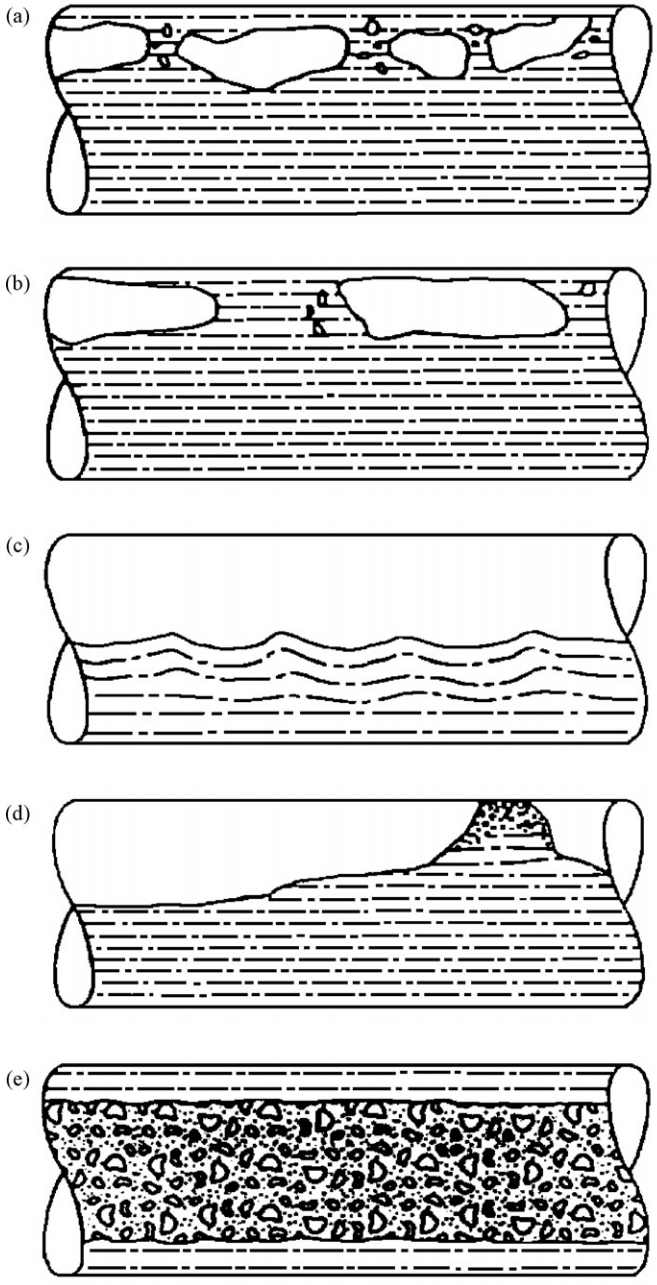

Fig. 1. Classification of flow patterns: (a) bubble flow—at high liquid velocity bubbles tend to flow in the upper part of the pipe; (b) plug flow—asymmetric nose bullet shaped bubbles occur; (c) wavy flow—at increased gas velocity; (d) slug flow—further increase in gas velocity causes waves to touch the top of the pipe and liquid is carried by the gas; (e) annular flow—at very high gas flow rate the slug becomes penetrated with a gas core and the flow becomes annular.

influenced by the turbulence levels and hence it is equally important to have knowledge of the spatial distribution of turbulent kinetic energy and the energy dissipation rates, although these are more difficult to measure experimentally, particularly in multiphase flow situations. Multiphase CFD models are gaining in importance as a tool that can shed insight on various chemical and mineral processes, provided they are validated against a good set of experimental data. Such an approach uses numerical techniques for solving the volume averaged conservation equations for a given flow geometry and boundary conditions, thereby implementing models for capturing phenomena like turbulence, interphase interactions for momentum, heat and mass transfer as relevant for the specific problem.

3.1. Mass conservation equation

The numerical simulations presented are based on the two-fluid, Eulerian–Eulerian model. The Eulerian modeling framework is based on ensemble-averaged mass and momentum transport equations for each phase. Regarding the liquid phase (α_l) as the continuum and the gaseous phase (bubbles) as the dispersed phase (α_g), these equations without interface mass transfer can be written in standard form as follows:

Continuity equation of the liquid phase:

$$\frac{\partial}{\partial t}(\rho_l \alpha_l) + \nabla \cdot (\rho_l \alpha_l \mathbf{u}_l) = 0 \tag{1}$$

Continuity equation of the gas phase:

$$\frac{\partial}{\partial t}(\rho_g \alpha_g f_i) + \nabla \cdot (\rho_g \alpha_g \mathbf{u}_g f_i) = S_i \tag{2}$$

where f_i is the volume fraction of bubbles of group i ($f_i = \alpha_{gi}/\alpha_g$) and S_i is a source term that takes into account the death and birth of bubbles caused by coalescence and break-up processes. With the above consideration of zero interphase mass transfer, it is clear that $S_i = 0$ under the assumption of constant and uniform bubble size. In this case S_i is calculated as

$$S_i = \mathrm{B}_i^{\mathrm{B}} + \mathrm{B}_i^{\mathrm{C}} - \mathrm{D}_i^{\mathrm{B}} - \mathrm{D}_i^{\mathrm{C}} \tag{3}$$

where i varies from 1 to N ($i = 1, 2, \ldots, N$) and terms on the right hand side B^{B}, B^{C}, D^{B} and D^{C} are respectively, the '*birth*' and '*death*' due to break-up and coalescence of bubbles. The production rates due to coalescence and break-up and the death rate to coalescence and break-up of bubbles formulated as

$$\mathrm{B}_i^{\mathrm{C}} = \frac{1}{2}\sum_{k=1}^{N}\sum_{l=1}^{N}\chi_{i,\mathrm{kl}} n_i n_j; \quad \mathrm{D}_i^{\mathrm{C}} = \sum_{j=1}^{N}\chi_{\mathrm{ij}} n_i n_j;$$

$$\mathrm{B}_i^{\mathrm{B}} = \sum_{j=i+1}^{N}\Omega(V_j : V_i) n_j; \quad \mathrm{D}_i^{\mathrm{B}} = \Omega_i n_i \tag{4}$$

The bubble number density n_i is related to the gas volume fraction α_g by: $\alpha_g f_i = n_i V_i$ where V_i is the corresponding volume of a bubble of group i. It is necessary to provide individual models for each of the break-up and coalescence processes as it depends on the mechanisms and are sensitively dependent on the presence of surfactants and turbulence levels, etc. These models are discussed next.

The break-up of bubbles in turbulent dispersions employs the model developed by Luo and Svendsen [20]. Binary break-up of the bubbles is assumed and the model is based on the theories of isotropic turbulence. The break-up rate of bubbles of volume V_j into volume sizes of V_i ($=V f_{\mathrm{BV}}$) can be obtained as

$$\frac{\Omega(V_j : V_i)}{(1-\alpha_g) n_j} = C\left(\frac{\in}{d_j^2}\right)^{1/3} \int_{\zeta_{\min}}^{1} \frac{(1+\zeta)^2}{\zeta^{11/3}} \exp \times \left(-\frac{12 c_f \sigma}{\beta \rho_l \in^{2/3} d_j^{5/3} \zeta^{11/3}}\right) d\zeta \tag{5}$$

where $\in$ is the rate of energy dissipation per unit of liquid mass; $\zeta = \lambda/d_j$ is the size ratio between an eddy and a particle in the inertial sub-range and consequently $\zeta_{\min} = \lambda_{\min}/d_j$; C and β are determined, respectively, from fundamental consideration of drops or bubbles

Table 1
Diameter of each bubble class tracked in the simulation

Class index	Bubble diameter, d_i (mm)
1	1.45
2	2.35
3	3.25
4	4.15
5	5.05
6	5.95
7	6.85
8	7.75
9	8.65
10	9.55

breakage in turbulent dispersion systems to be 0.923 and 2.0 in Luo and Svendsen [20]; and c_f is the increase coefficient of surface area:

$$c_f = [f_{BV}^{2/3} + (1 - f_{BV})^{2/3} - 1]$$

where f_{BV} is the breakage volume fraction.

The coalescence of two bubbles is assumed to occur in three steps. The first step where the bubbles collide and trap a layer of liquid between them, a second step where this liquid layer drains until it reaches a critical thickness, and a last step during which this liquid film disappears and the bubbles coalesce. The collisions between bubbles may be caused by turbulence, buoyancy or laminar shear. Only the first cause of collision (turbulence) is considered in the present model. Indeed collisions caused by buoyancy cannot be taken into account as all the bubbles from each class move at the same speed. The coalescence rate considering turbulent collision taken from Prince and Blanch [21] can be expressed as

$$\chi = \frac{\pi}{4}[d_i + d_j]^2(\mathbf{u}_{ti}^2 + \mathbf{u}_{tj}^2)^{1/2} \exp\left(-\frac{t_{ij}}{\tau_{ij}}\right) \quad (6)$$

where τ_{ij} is the contact time for two bubbles given by $(d_{ij}/2)^{2/3}/\in^{1/3}$ and t_{ij}, the time required for two bubbles, having diameters d_i and d_j to coalesce is estimated to be $\{(d_{ij}/2)^3\rho_l/16\sigma\}^{1/2}\ln(h_0/h_j)$. The equivalent diameter d_{ij} is calculated as suggested by Chesters and Hoffman [22]: $d_{ij} = (2/d_i + 2/d_j)^{-1}$. The parameters h_0 and h_j represent the film thickness when collision begins and critical film thickness at which rupture occurs, respectively. The turbulent velocity $\mathbf{u}_t$ in the inertial sub-range of isotropic turbulence [23] is:

$$\mathbf{u}_t = 1.4 \in^{1/3} d^{1/3}.$$

3.2. Momentum transfer equations

The momentum conservation for multiphase flows is described by the volume averaged momentum equation as follows:

$$\frac{\partial}{\partial t}(\rho_k \alpha_k u_k) + \nabla \cdot (\rho_k \alpha_k \mathbf{u}_k \mathbf{u}_k) = -\alpha_k \nabla p + \rho_k \alpha_k g - \nabla(\alpha_k \tau_k) + \boldsymbol{F}_{km} \quad (k, m = l, g) \quad (7)$$

where $\mathbf{u}$ is the volume averaged velocity vector, p is the pressure, g is the gravity, τ_k is the phase shear stress tensor ($\tau_k = -\mu_k(\nabla \mathbf{u}_k + (\nabla \mathbf{u}_k)^T)$) and $\boldsymbol{F}_{km}$ is the interphase force term. The terms on the right-hand side describes the following forces acting on the phase k: the pressure gradient, gravity, the viscous stress term and interphase momentum forces combined in $\boldsymbol{F}_{km}$. The pressure is defined equal in both phases. The effective viscosity μ_k of the viscous stress term consists of the laminar viscosity and an additional turbulent part in case of turbulence. The total interfacial force acting between two phases may arise from several independent physical effects:

$$\boldsymbol{F}_{km} = \boldsymbol{F}_D + \boldsymbol{F}_L + \boldsymbol{F}_{VM} + \boldsymbol{F}_{WL} + \boldsymbol{F}_{TD} \quad (8)$$

The forces indicated above respectively represent the interphase drag force $\boldsymbol{F}_D$, lift force $\boldsymbol{F}_L$, virtual mass force $\boldsymbol{F}_{VM}$, wall lubrication force $\boldsymbol{F}_{WL}$, and turbulence dispersion force $\boldsymbol{F}_{TD}$. Detailed descriptions of each of these forces can be found in Anglart and Nylund [24]; Lahey and Drew [25] and Joshi [26]. While the mechanistic reasoning for the existence of such forces arises from detailed quantitative study of single droplets/bubbles, the precise form and relative importance of such forces in the presence of many bubbles is often proposed empirically as closure relations and must be validated against careful experiments. This is a challenging task since many mechanisms must be modeled often using limited macroscopic data on multiphase flows such as pressure drops, average volume fraction of a phase etc. In the present hydrodynamic model all forces except virtual mass force (the drag force, lift force, wall lubrication force and turbulence dispersion forces) are investigated.

The origin of the drag force is due to the resistance experienced by a body moving in the liquid. Viscous stress creates skin drag and pressure distribution around the moving body creates form drag.

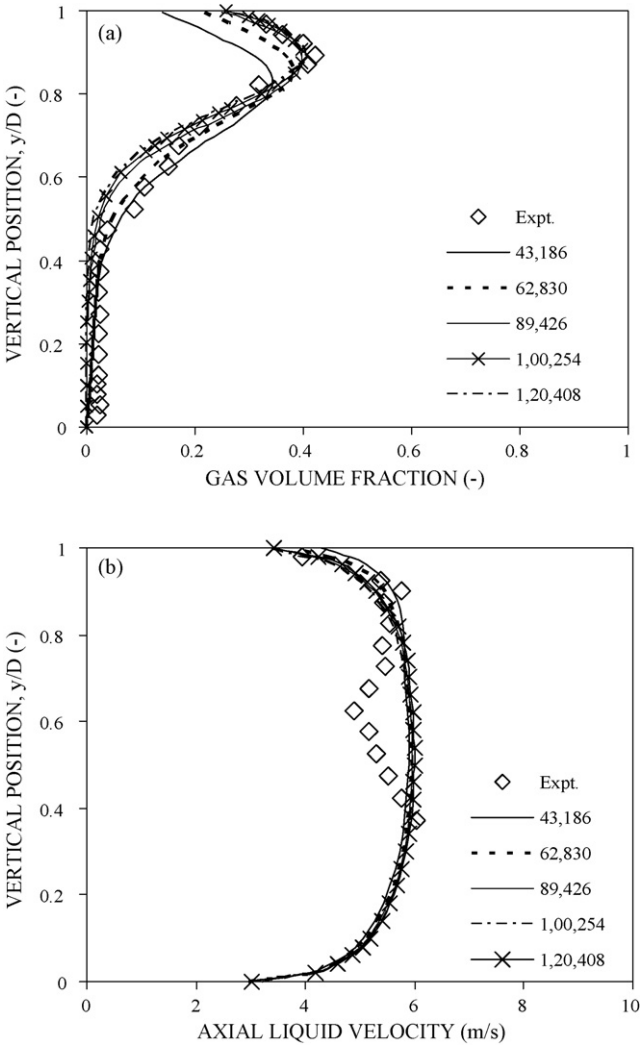

Fig. 2. Effect of grid size on gas volume fraction and axial liquid velocity.

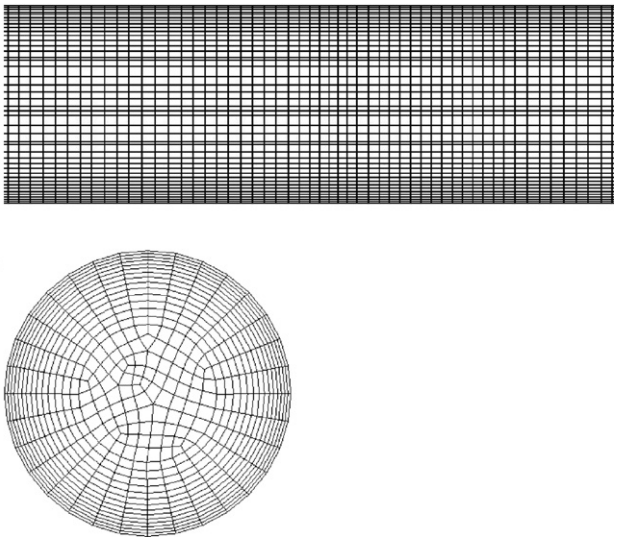

Fig. 3. Computational grid (a) r–z plane and (b) r–θ plane.

The drag force density is written in the following form:

$$\boldsymbol{F}_{\mathrm{D}} = \frac{3}{4} C_{\mathrm{D}} \alpha_{\mathrm{d}} \rho_{\mathrm{c}} \frac{1}{d_{\mathrm{b}}} |\mathbf{u}_{\mathrm{c}} - \mathbf{u}_{\mathrm{d}}| (\mathbf{u}_{\mathrm{c}} - \mathbf{u}_{\mathrm{d}}) \tag{9}$$

where C_{D} is the drag coefficient taking into account the character of the flow around the bubble and d_{b} is the bubble diameter. The drag coefficient C_{D} in Eq. (9) has been modeled using Ishii-Zuber [27] drag model.

The lift force considers the interaction of the bubble with the shear field of the liquid. It acts perpendicular to the main flow direction and is proportional to the gradient of the liquid velocity field. The lift force in terms of the slip velocity and the curl of the liquid phase velocity can be modeled as [28–31]:

$$\boldsymbol{F}_{\mathrm{L}}^{\mathrm{c}} = -\boldsymbol{F}_{\mathrm{L}}^{\mathrm{d}} = C_{\mathrm{L}} \alpha_{\mathrm{d}} \rho_{\mathrm{c}} (\mathbf{u}_{\mathrm{d}} - \mathbf{u}_{\mathrm{c}}) \times \nabla \times \mathbf{u}_{\mathrm{c}} \tag{10}$$

where C_{L} is the lift coefficient and the subscripts c and d stands for the continuous and dispersed phases. The sign of this force depends on the orientation of slip velocity vector. For example, it is known that in upward pipe flows this force pushes bubbles towards the wall. When flow is downward, it pushes bubbles to the pipe center. In the present work, a constant value of the lift coefficient $C_{\mathrm{L}} = -0.2$ has been used. The value used is within the range of values suggested in the literature [31]. In the horizontal pipe flows, the negative lift coefficient has been used because this force pushes bubbles to the pipe center.

The turbulent dispersion force, derived by Lopez de Bertodano [32], is based on the analogy with molecular movement. It approximates a turbulent diffusion of the bubbles by the liquid eddies. It is formulated as

$$\boldsymbol{F}_{\mathrm{TD}}^{\mathrm{c}} = -\boldsymbol{F}_{\mathrm{TD}}^{\mathrm{d}} = -C_{\mathrm{TD}} \rho_{\mathrm{c}} k_{\mathrm{c}} \nabla \alpha_{\mathrm{c}} \tag{11}$$

where k_{c} is the liquid turbulent kinetic energy per unit of mass. The turbulent dispersion coefficient of $C_{\mathrm{TD}} = 0.5$ was found to give the good results which is in the recommended range of 0.1–1.0 [32].

The origin of the wall lubrication force is due to the fact that liquid flow rate between bubble and the wall is lower than between the bubble and the outer flow. This result in a hydrodynamics pressure difference driving bubble away from the wall. This force density is approximated as [33]:

$$\boldsymbol{F}_{\mathrm{WL}}^{\mathrm{c}} = -\boldsymbol{F}_{\mathrm{WL}}^{\mathrm{d}} = -\alpha_{\mathrm{g}} \rho_{\mathrm{l}} \frac{(\mathbf{u}_{\mathrm{r}} - (\mathbf{u}_{\mathrm{r}} n_{\mathrm{w}}) n_{\mathrm{w}})^2}{d_{\mathrm{b}}} \max \left[C_1 + C_2 \frac{d_{\mathrm{b}}}{y_{\mathrm{w}}}, 0 \right] n_{\mathrm{w}} \tag{12}$$

here, $\mathbf{u}_{\mathrm{r}} = \mathbf{u}_{\mathrm{c}} - \mathbf{u}_{\mathrm{d}}$ is the relative velocity between phases, d_{b} is the disperse phase mean diameter, y_{w} is the distance to the nearest wall, and n_{w} is the unit normal pointing away from the wall. Hence the force acts to push the disperse phase away from the wall. The wall lubrication constants C_1 and C_2, as suggested by Antal et al. [33], are −0.01 and 0.05, respectively. The local bubble Sauter mean diameter based on the calculated values of the scalar fraction f_i and discrete bubble sizes d_i can be deduced from:

$$d_{\mathrm{b}} = \frac{1}{\sum_i f_i / d_i} \tag{13}$$

3.3. Turbulence equations

Turbulence is taken into consideration for the continuous phase. The dispersed gas phase is modeled as laminar flow, but the influence of the dispersed phase on the turbulence of the continuous phase is taken into account with Sato's additional term [34]. The well-known single-phase turbulence models are usually used to model turbulence of the liquid phase in Eulerian–Eulerian multiphase simulations. In the present case the standard k–ε model published by Launder and Spalding [35] is used. The governing equations for the turbulent kinetic energy k and turbulent dissipation ε are:

$$\frac{\partial}{\partial t}(\rho_{\mathrm{l}} \alpha_{\mathrm{l}} k) + \frac{\partial}{\partial x_i}(\rho_{\mathrm{l}} \alpha_{\mathrm{l}} \mathrm{u}_{\mathrm{l}} k) = \frac{\partial}{\partial x_i}\left(\alpha_{\mathrm{l}} \left(\mu_{\mathrm{l}} + \frac{\mu_{\mathrm{l,tur}}}{\sigma_k} \right) \frac{\partial k}{\partial x_i} \right) + \alpha_{\mathrm{l}} (G - \alpha_{\mathrm{l}} \rho_{\mathrm{l}} \in_{\mathrm{l}}) \tag{14}$$

$$\frac{\partial}{\partial t}(\rho_{\mathrm{l}} \alpha_{\mathrm{l}} \in_{\mathrm{l}}) + \frac{\partial}{\partial x_i}(\rho_{\mathrm{l}} \alpha_{\mathrm{l}} \mathrm{u}_{\mathrm{l}} \in_{\mathrm{l}}) = \frac{\partial}{\partial x_i}\left(\alpha_{\mathrm{l}} \left(\mu_{\mathrm{l}} + \frac{\mu_{\mathrm{l,tur}}}{\sigma_{\in}} \right) \frac{\partial \in_{\mathrm{l}}}{\partial x_i} \right) + \alpha_{\mathrm{l}} \frac{\in_{\mathrm{l}}}{k} (C_{\varepsilon 1} G - C_{\varepsilon 2} \alpha_{\mathrm{l}} \rho_{\mathrm{l}} \in_{\mathrm{l}}) \tag{15}$$

where $C_{1\in}, C_{2\in}, C_\mu, \sigma_k, \sigma_\in$ are the standard k–$\in$ model constants and G is the turbulence production term. This standard model is used without any further modifications.

Using the standard k–$\in$ model the turbulent viscosity of the continuous phase is calculated by

$$\mu_{\alpha,\mathrm{tur}} = C_\mu \rho_{\mathrm{c}} \frac{k_{\mathrm{c}}^2}{\in_{\mathrm{c}}} \tag{16}$$

For the continuous liquid phase, a k–ε model is applied with its standard constants: $C_{\in 1} = 1.44$, $C_{\in 2} = 1.92$, $C_\mu = 0{:}09$; $\sigma_k = 1$ and $\sigma_\in = 1.3$. The effective viscosity in Eq. (3) is then given by

$$\mu_{\alpha,\mathrm{eff}} = \mu_{\alpha,\mathrm{lam}} + \frac{\mu_{\alpha,\mathrm{tur}}}{\sigma_k} \tag{17}$$

4. Method of solution

The simulations were carried out as three dimensional transient flow pattern in a horizontal pipe with dimensions of 50.4×9000 mm ($r \times z$) using the commercial software CFX-5.7.1,

Table 2
Operating conditions

Geometry	Diameter 50.3 mm i.d., length 9.0 m
Gas phase	Air at 25 °C
Liquid phase	Water at 25 °C
Gas superficial velocity	0.2–1.0 m/s
Liquid superficial velocity	3.8–5.1 m/s
Average gas volume fraction	0.04–0.16

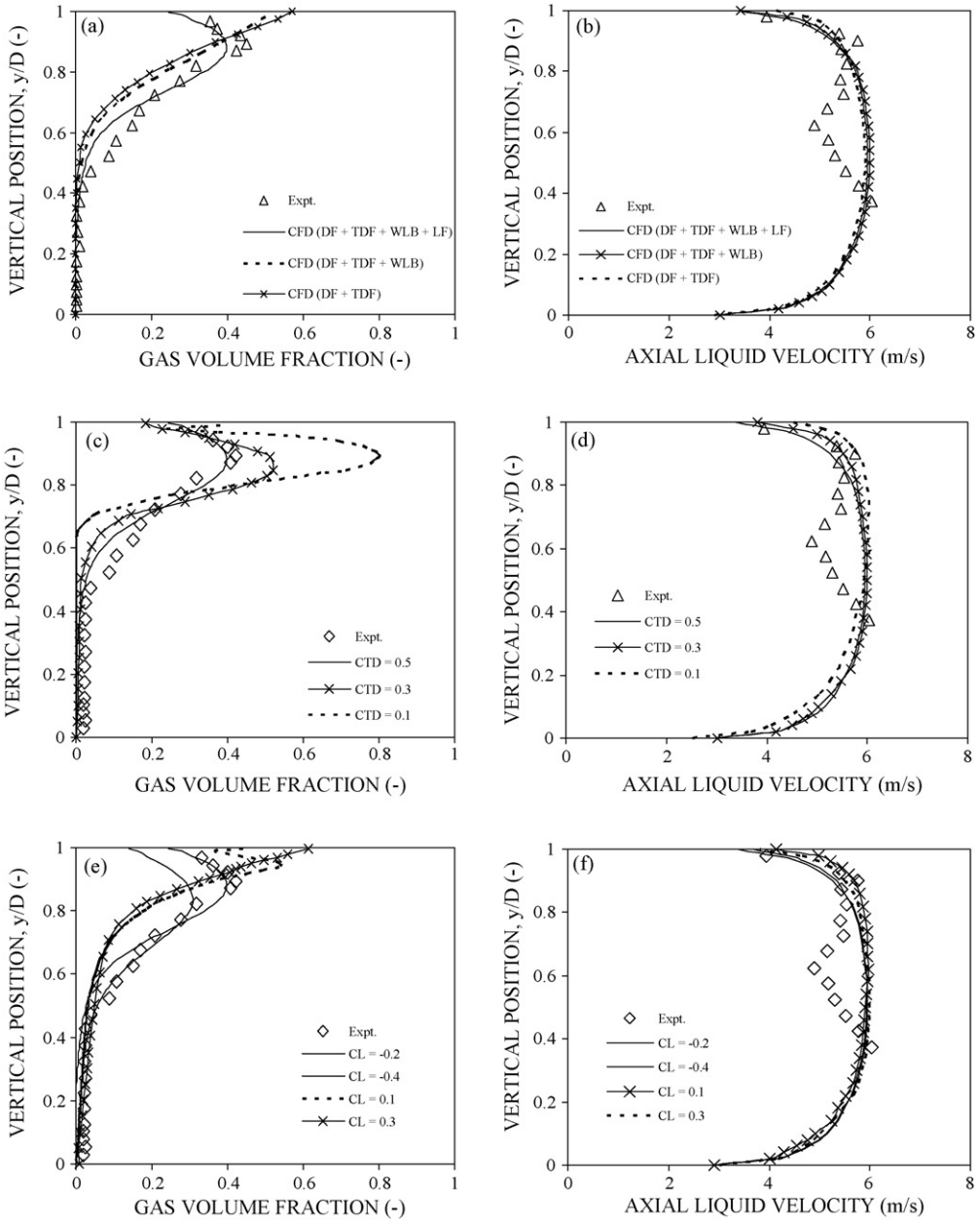

Fig. 4. Effects of Drag Force (DF), Turbulent Dispersion Force (TDF), Wall Lubrication force (WLB) and Lift Force (LF) are assessed by comparing simulated and the experimental profile of gas volume fraction and axial liquid velocity at vertical position for superficial gas velocity of 0.42 m/s and superficial liquid velocity is 4.67 m/s and average gas volume fraction is 0.085: (a) and (b) effect of different interface forces on gas volume fraction and liquid velocity; (c) and (d) effect of dispersion coefficient (C_{TD}) on gas volume fraction and axial liquid velocity keep C_L (−0.2) as a constant; (e) and (f) effect of lift coefficient (C_L) on gas volume fraction and axial liquid velocity keep C_{TD} (0.5) as a constant.

which is based on an Eulerian–Eulerian description. Water was considered as the continuous phase, and air was considered as the dispersed phase. In the present study, bubbles ranging from 1 to 10 mm diameter are equally divided into 10 classes (see Table 1). The MUltiple Size Group (MUSIG) model [36] has been used in CFX-5.7.1 to account for the non-uniform bubble size distribution in a gas–liquid mixture. The discrete bubble sizes prescribed in the dispersed phase were tracked by solving an additional set of 10 transport equations, these equations were progressively coupled with the flow equations during the simulations. Instead of considering 11 different complete phases, it was assumed that each bubble class travels at the same mean algebraic velocity to reduce the computational time and resource. This therefore results in 10 continuity equations for the gas phase coupled with a single continuity equation for the liquid phase. In addition simulations were carried out with constant bubble size of 2 mm using k–ε.

Solution to the two sets of governing equations for the balances of mass and momentum of each phase was sought. Discretization of the partial differential equations is based on the conservative finite volume method. Computational grid is based on the unstructured set of blocks each containing structured grid. The structured grid within each block is generated using general curvilinear coordinates ensuring accurate representation of the flow boundaries. In order to select an adequate grid resolution, the effect of changing grid size was investigated. Several simulations were carried out using progressively larger number of grid points of 43186; 62830; 89426, 100254 and 120408. Sample grid sensitivity results are shown in Fig. 2. It can be seen that there is practically no change

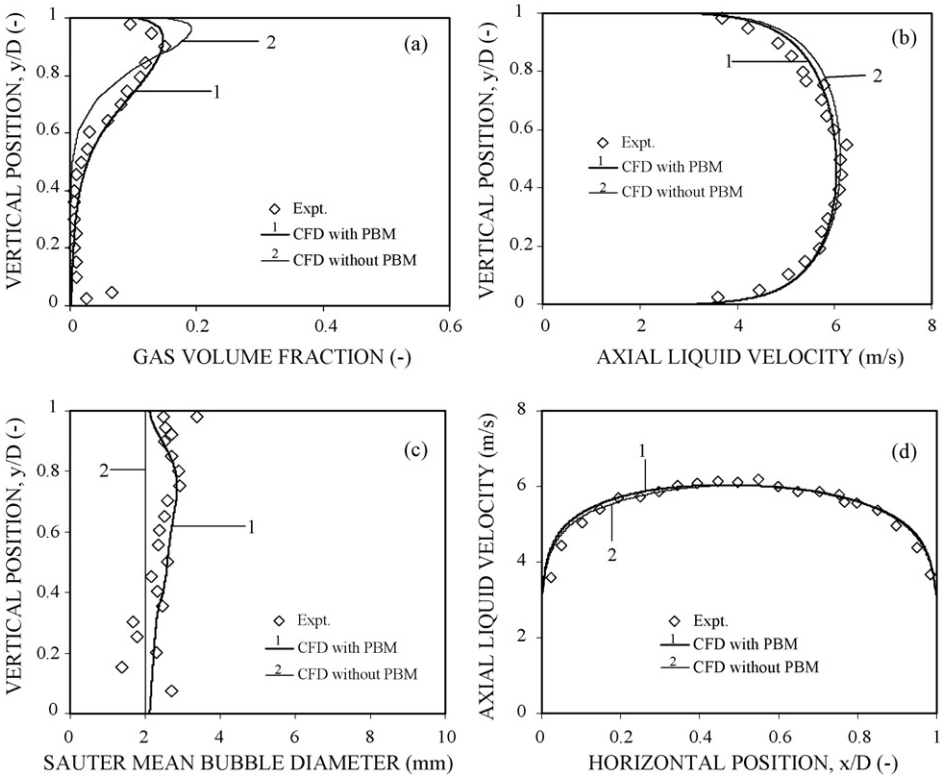

Fig. 5. Comparison of predicted and experimental data of Kocamustafaogullari and Wang [10] for superficial gas velocity of 0.25 m/s and superficial liquid velocity is 5.1 m/s and volume fraction is 0.043: (a) gas volume fraction at vertical position (b) axial liquid velocity at vertical position (c) Sauter mean bubble diameter at vertical position and (d) axial liquid velocity at horizontal position.

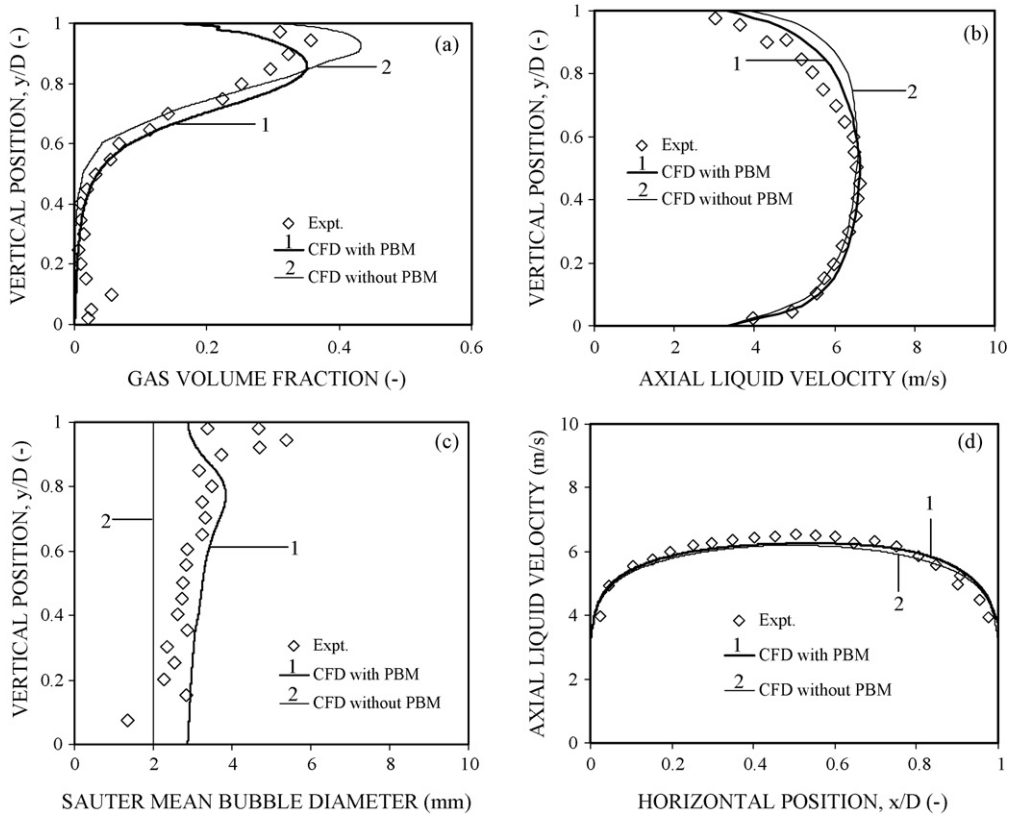

Fig. 6. Comparison of predicted and experimental data of Kocamustafaogullari and Wang [10] for superficial gas velocity of 0.50 m/s and superficial liquid velocity is 5.1 m/s and volume fraction is 0.080: (a) gas volume fraction at vertical position (b) axial liquid velocity at vertical position (c) Sauter mean bubble diameter at vertical position and (d) axial liquid velocity at horizontal position.

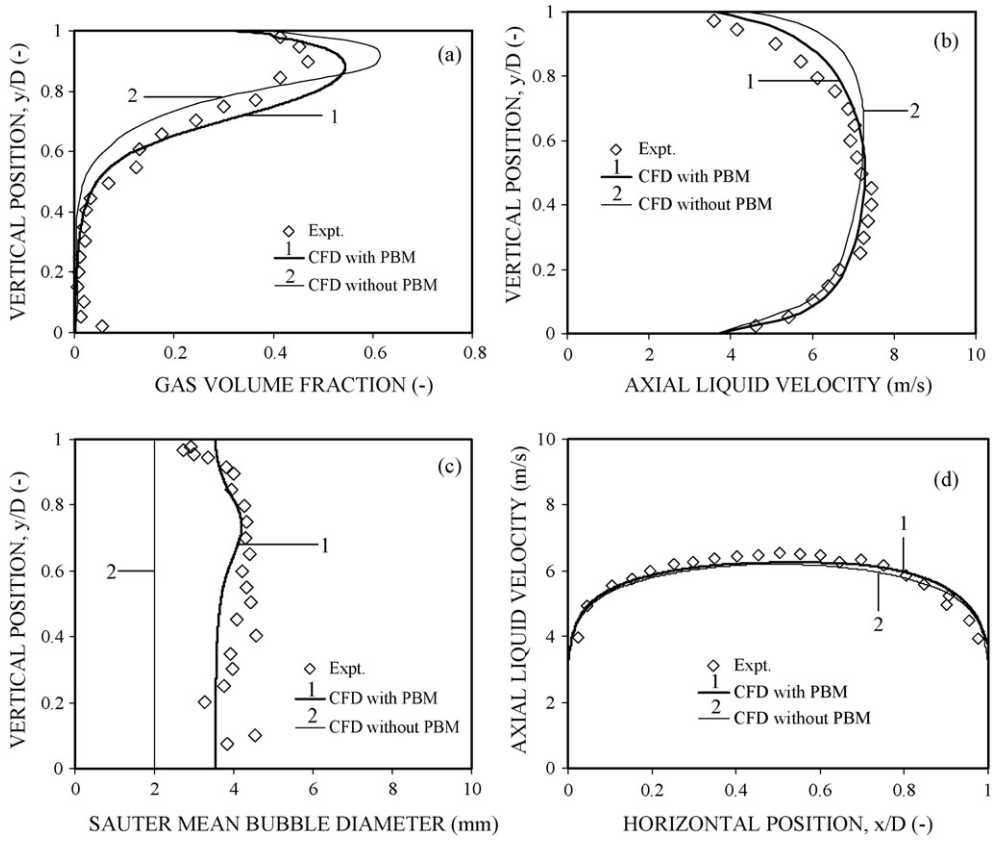

Fig. 7. Comparison of predicted and experimental data of Kocamustafaogullari and Wang [10] for superficial gas velocity of 0.80 m/s and superficial liquid velocity is 5.1 m/s and volume fraction is 0.139: (a) gas volume fraction at vertical position (b) axial liquid velocity at vertical position (c) Sauter mean bubble diameter at vertical position and (d) axial liquid velocity at horizontal position.

in the gas volume fraction and liquid velocity profiles when the grid size increased beyond 89426. In view of the observed effect of grid size, the simulations have been carried out by using 89426 grid points and the grid structure is shown in Fig. 3. Initial simulations were carried out with a coarse mesh to obtain an initial converged solution and to obtain an indication of where a high mesh density was needed. However, a dense mesh required additional computational effort. In both the models, the time step 0.005 s was used. Under-relaxation factors between 0.6 and 0.7 were adopted for all flow quantities. Pressure was never under-relaxed, as required by the SIMPLEC algorithm. The hybrid-upwind discretization scheme was used for the convective terms. At the pipe inlet, uniform gas and liquid velocities and average volume fractions have been specified. At the pipe outlet, a relative average static pressure of zero was specified. For initiating the numerical solution, average volume fraction and parabolic liquid velocity profile are specified. The operating conditions are summarized in Table 2.

5. Results and discussion

The simulations were carried out to obtain results under fully developed bubble flow conditions in the 50.4 mm i.d. and 9000 mm long horizontal pipe lines using CFX for air-water system. Liquid (V_L) and gas (V_G) volumetric superficial velocities varied in the range from 3.8 to 5.1 m/s and 0.2 to 1.0 m/s, respectively, and average volume fractions varied in the range from 4 to 16%. The simulation results were compared with the experimental data of Kocamustafaogullari and Wang [10], Kocamustafaogullari and Huang [12] and Iskandrani and Kojasoy [13]. The simulation results are taken at near outlet of the pipe and along a vertical and horizontal line passing through the centre of the pipe axis. Here, y/D and x/D are the normalized vertical and horizontal positions in the pipe.

5.1. Sensitivity analysis on gas volume fraction profile

In order to understand the effect of different forces, the numerical simulations have been carried out for three different cases. In the first case, the 3D simulations are carried out taking drag force and turbulent dispersion force into account. The predicted volume fraction profile shows a peak in the top of the pipe, where gas bubbles tend to migrate toward the upper wall. In second case, the simulations were carried out including drag, turbulent dispersion force and wall lubricant force. The result does not show any significant change and the behavior was basically same. In third case, when the drag force, the lift force and turbulent dispersion force were incorporated, the gas volume fraction profile shows good agreement with experimental data. Fig. 4(a) shows the comparison of the gas volume fraction for all these cases. Fig. 4(b) shows the comparison of the axial liquid velocity prediction for above all cases; it can be observed that there is no significant change in the predictions. Further, to see the sensitivity of turbulent dispersion coefficient (C_{TD}) and lift coefficient (C_L) on gas volume fraction various simulations were carried out and results were shown in Fig. 4. For Fig. 4(c), the lift coefficient ($C_L = -0.2$) is kept constant whereas the turbulent dispersion coefficient (C_{TD}) is treated as a parameter. It can be observed from Fig. 4(c) that the gas is well disperses as turbulent dispersion coefficient is increased. In Fig. 4(e), the tur-

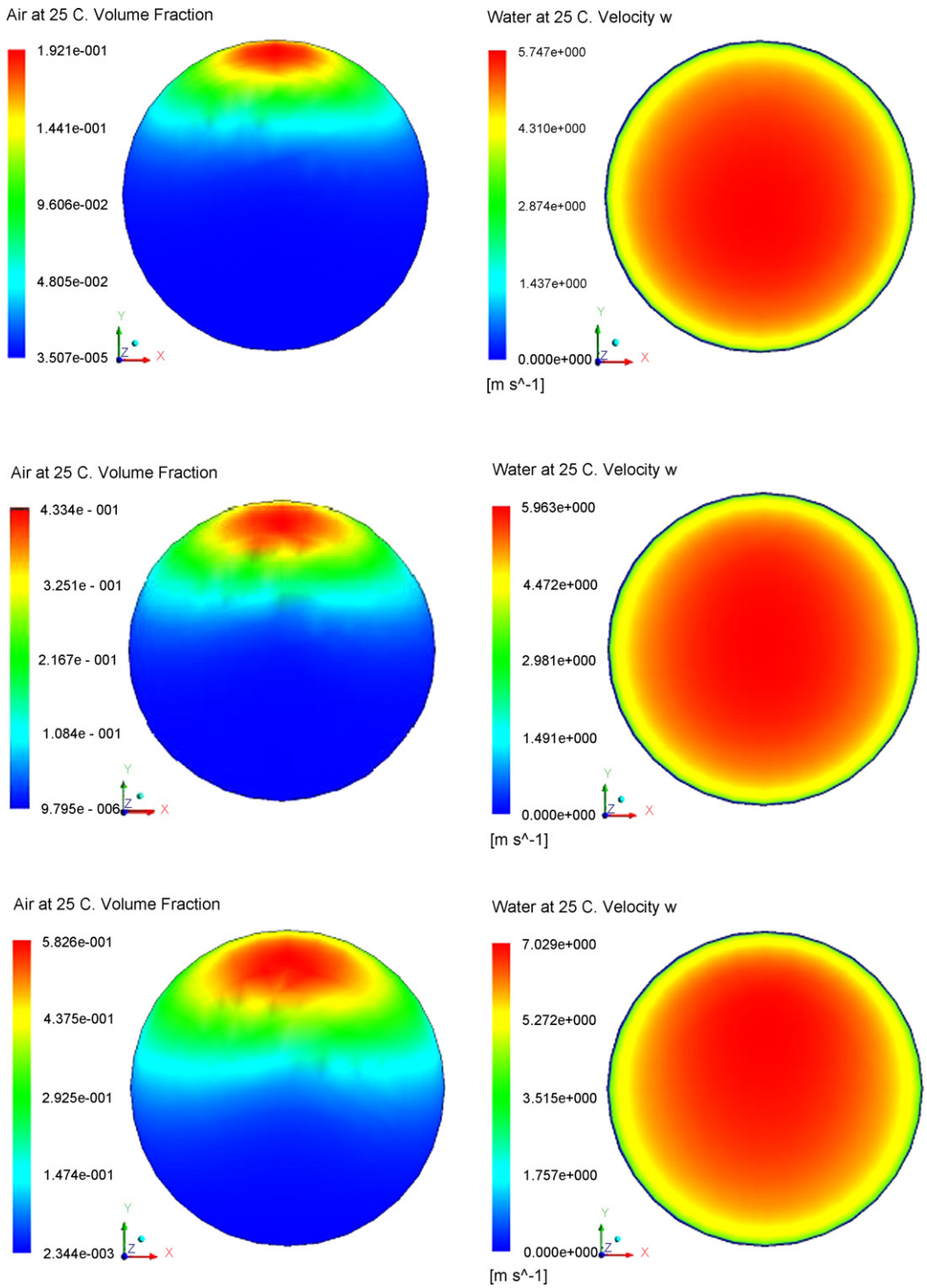

Fig. 8. Contour plots of simulated gas volume fraction and axial liquid velocity at outlet of the pipe (a) and (b) $V_G = 0.25$ m/s, $V_L = 5.1$ m/s, $\alpha_g = 0.043$; (c) and (d) $V_G = 0.50$ m/s, $V_L = 5.1$ m/s, $\alpha_g = 0.08$; (e) and (f) $V_G = 0.80$ m/s, $V_L = 5.1$ m/s, $\alpha_g = 0.139$.

bulent dispersion coefficient ($C_{TD} = 0.5$) is kept constant whereas the lift coefficient (C_L) is treated as a parameter. It can be seen from figure that the gas volume fraction profiles shows a peak in the top of the pipe, where gas bubbles tend to migrate toward the upper wall for the positive lift coefficient. For the negative lift coefficient the volume fraction profile shows same trend of the experimental data. From these simulations, we found that the $C_L = -0.2$ and $C_{TD} = 0.5$ gives good match of predicted and observed profiles.

5.2. Gas volume fraction profiles

Figs. 5–7(a) shows the comparison of the predicted gas volume fraction profiles with two different models (k–ε model with constant bubble size and k–ε model with bubble size distribution) and the experimental data obtained from double sensor resistivity probe [12] for different superficial gas velocities (0.25, 0.50, and 0.80 m/s). It can be seen from the figures that the local gas volume fraction profile shows a peak at the top of the pipe, where gas bub-

bles tend to migrate toward the upper wall for all the superficial gas velocity. This peak can be attributed to the increased hydraulic resistance of the liquid path between the bubble and the wall which may cause a sharp decline in volume fraction. The similar observation was made experimentally by Kocamustafagullari and Wang [10], Kocamustafaogullari and Huang [12], and Iskandrani and Kojasoy [13]. Further, it can be seen that the predictions of k–ε with population model shows good agreement with experimental profiles. The k–ε model with constant bubble size shows underpredicts and relative mean and maximum errors are ±5% and ±17% respectively. Fig. 8(a), (c) and (e) shows contour plots of simulated local gas volume fraction for different superficial gas velocities at outlet of the pipe. It can be seen from these figures, that most of the bubbles migrated towards the top of the pipe.

5.3. Mean axial liquid velocity

Figs. 5–7(b) show the comparison of predicted and experimental data of axial liquid velocity profiles for different superficial gas and liquid velocities. If only a single liquid phase moves in the pipe, the liquid velocity in the pipe top region will be equal to the velocity in the bottom region, exhibiting a perfect axi-symmetry. But these results show that the axial liquid velocity profile has a slight degree of asymmetry due to the presence of gas flow. The degree of asymmetry decreases with increasing liquid flow or decreasing gas flow. For increasingly higher gas velocities (Figs. 5–7(b)), the liquid velocity in the upper region of the pipe is slightly lower than in the lower region. This could be attributed to larger volume fraction of gas in the upper region which is the reason for the asymmetric distribution of the liquid velocity. The slip velocity, because of the big difference in densities between phases, is an important characteristic of two-phase flow. It is evident that the liquid phase occupies a dominant position in the pipe bottom section where the movement of the gas phase is controlled by the liquid phase with a little slip velocity between them. Whereas, in the top part of the pipe, there is a large slip velocity. The reason for this big slip velocity is that gas moves with less limitation by liquid and liquid velocity tends to decrease due to the boundary condition. An interesting feature of the velocity profile is that the velocity distribution within the bottom liquid layer resembles closely a fully developed turbulent pipe flow profile irrespective of the liquid and gas superficial velocities. The model prediction of axial liquid velocity shows relative mean and maximum errors are ±5%, and ±14%, respectively. Figs. 5–7(b) show a mild degree of asymmetry in the vertical direction, the two-dimensional variations of the axial liquid velocity, shown in Fig. 8(b), (d) and (f), shows the extent of asymmetry in the liquid velocity is indeed quite small over the entire cross-plane.

5.4. Sauter bubble mean diameter

Figs. 5–7(d) show the comparison of predicted and the experimental data of the local mean bubble diameter distribution. Good agreement was achieved against the measured bubble size with k–ε model with population balance model. It can be observed that the local mean bubble size in the top region is larger than in the bottom region. In the top region, gas volume fraction is higher, because of the most of the bubble are at the top of the pipe due to buoyancy Further, it can be seen that the bubble size distribution is almost uniform in the pipe cross-section.

5.5. Effect of flow variables

To investigate the effect of the superficial gas velocity on the profiles of gas volume fraction and axial liquid velocity, various simulations were carried out and the results are shown in Fig. 9. The

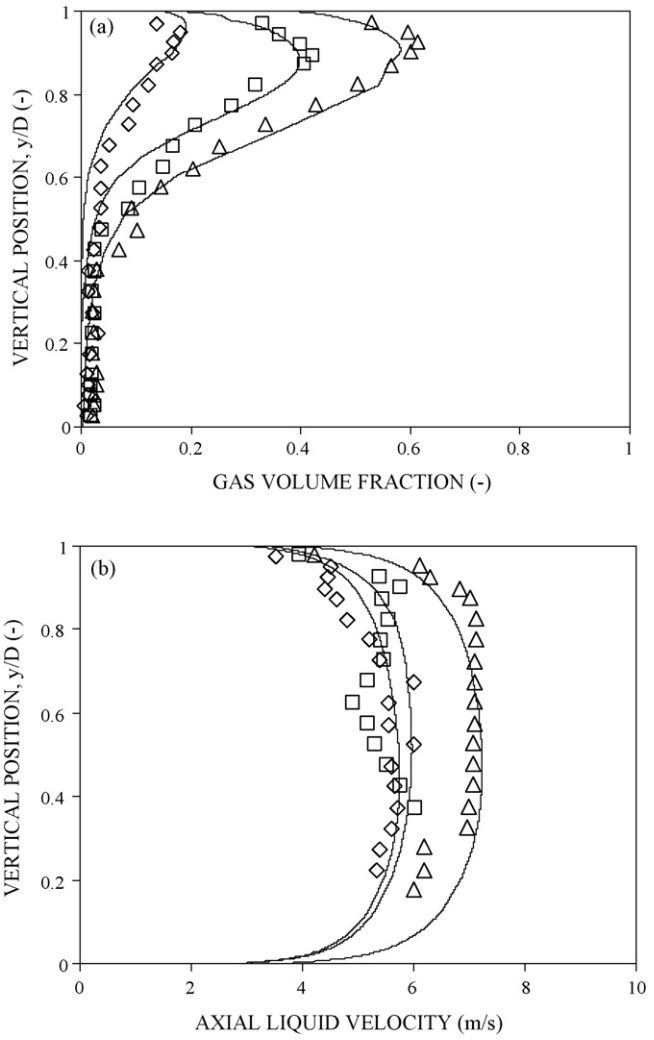

Fig. 9. The effect of superficial gas velocity on (a) gas volume fraction and (b) axial liquid velocity: ◊: V_G = 0.213 m/s; □: V_G = 0.42 m/s; and Δ: V_G = 0.788 m/s for constant V_L = 4.67 m/s.

superficial liquid velocity (V_L) is kept constant while the superficial gas velocity (V_G) is treated as a parameter. It can be seen from Fig. 9 that the CFD simulations show good agreement with experimental data for all the superficial gas velocities. From this Fig. 9(a), it can be observed that the gas volume fraction profiles for a given superficial liquid velocity show that with an increase in superficial gas velocity, the local gas volume fraction increases. In the bottom part of the pipe, the local gas volume fraction decreases with increasing the superficial gas velocity. The gas volume fraction generally exhibits a distinct peak near the top wall for all the flow conditions and the trend of the profiles appear to be same with increasing superficial gas velocity. Fig. 9(b) shows the comparison between the CFD predictions and experimental data of axial liquid velocity. It can be seen from figure that the axial liquid velocity profiles shows good agreement with experimental data.

The effect of superficial liquid velocity on the local gas volume fraction and axial liquid velocity at a constant superficial gas velocity is shown in Fig. 10. It can be observed from Fig. 10(a) that the CFD predictions show good agreement of gas volume fraction with experimental data [13]. From this figure, it can be observed that increasing superficial liquid velocity is to disperse bubbles and flatten the gas volume fraction profile, thus shrinking the liquid layer. Further, it can be seen that the gas volume fraction peak decreases

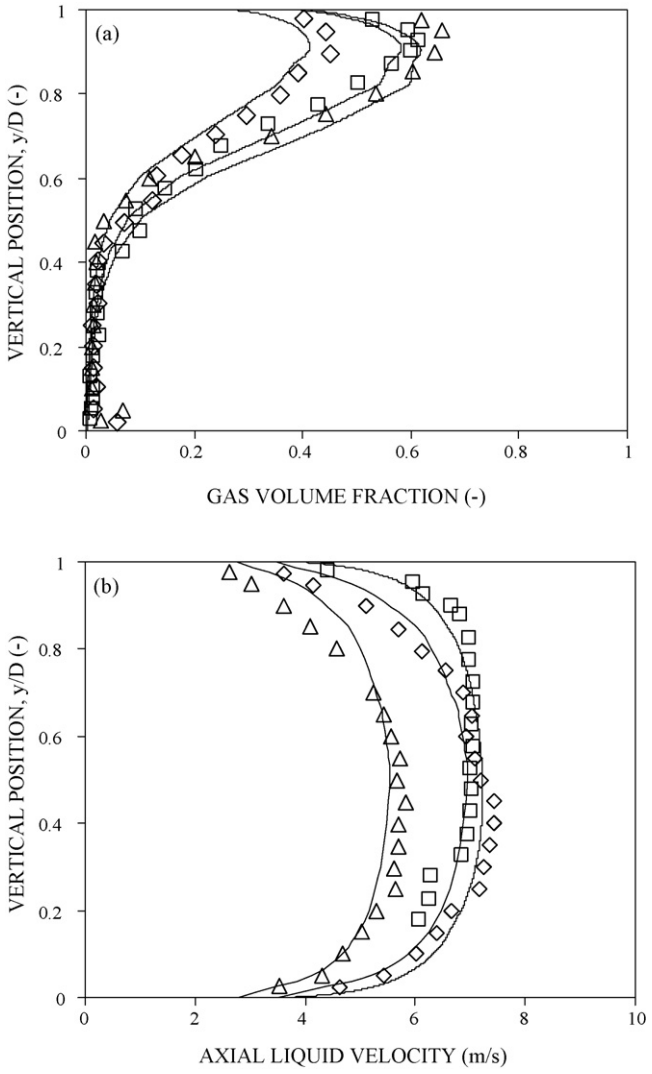

Fig. 10. The effect of superficial liquid velocity on (a) gas volume fraction and (b) axial liquid velocity: Δ: V_L = 3.8 m/s; □: V_L = 4.67 m/s; and ◊: V_L = 5.0 m/s for constant V_G = 0.8 m/s.

as the superficial liquid velocity increases. There is no noticeable difference observed in the peak positions of the gas volume fraction. It is evident that bubble boundary layer is most pronounced at high superficial liquid velocities. Fig. 10(b) shows that an increase in the superficial liquid velocity tends to make the liquid mean velocity profile develop toward a symmetric behavior. The agreement between the CFD model predictions and the experiments is poor at low liquid velocities and in the upper region of the pipe. It gets progressively better with increasing liquid velocity. One reason for this discrepancy might be the use of uniform bubble size in our simulation. At lower liquid velocities, the bubble size might be larger than the 2 mm that we have used in the simulation.

6. Conclusions

A comprehensive computational fluid dynamic model has been developed for horizontal two-phase pipe flows. A detailed comparison of a CFD simulation and the experimental data reported by Kocamustafaogullari and Wang [10], Kocamustafaogullari and Huang [12] and Iskandrani and Kojasoy [13] has been presented. Good quantitative agreement with the experimental data is obtained with two different models (i.e., k–ε with constant bubble size and k–ε model with population balance model) for wide range of superficial gas and liquid velocities (0.2–1.0 m/s and 3.8–5.1 m/s, respectively). The model prediction shows better agreement with the experimental data with population balance than constant bubble diameter predictions. The experimental and simulated results indicate that the gas volume fraction has local maxima near the upper pipe wall, and the profiles tend to flatten with increasing superficial liquid velocity. It was found that increasing the superficial gas velocity at fixed superficial liquid velocity would increase the local gas volume fraction. The simulation results were consistent with experimental observations from the literature. The axial liquid mean velocity showed a relatively uniform distribution except near the upper pipe wall. The flow in the bottom part of the pipe exhibits a fully developed turbulent pipe flow profile, whereas in the top of the pipe a different flow exists.

Acknowledgments

The authors gratefully acknowledge the financial support of the Natural Sciences and Engineering Research Council of Canada (NSERC) and Syncrude Canada Ltd. for this project.

References

[1] K. Ohba, T. Itoh, Light attenuation technique for void fraction measurement in two-phase bubbly flow. II. Experiment, Tech. Rep. Osaka Univ. 28 (1978) 495–506.
[2] S.K. Wang, S.J. Lee, Jones O.C.Jr., R.T. Lahey Jr., Three-dimensional turbulence structure and phase distribution measurements in bubbly two-phase flow, Int. J. Multiphase Flow 23 (1987) 327–340.
[3] I. Zun, Mechanism of bubble non-homogeneous distribution in two-phase shear flow, Nucl. Eng. Des. 118 (1990) 155–162.
[4] M. Lance, J.M. Bataille, Turbulence in the liquid phase in a uniform bubbly air-water flow, J. Fluid Mech. 222 (1991) 95–118.
[5] T.J. Liu, S.G. Bankoff, Structure of air-water bubbly flow in a vertical pipe. I. Liquid mean velocity and turbulence measurements, Int. J. Heat Transfer 36 (1993) 1049–1060.
[6] T.J. Liu, S.G. Bankoff, Structure of air-water bubbly flow in a vertical pipe. II. Void fraction, bubble velocity and bubble size distribution, Int. J. Heat Transfer 36 (1993) 1061–1072.
[7] T. Hibiki, S. Hogsett, M. Ishii, Local measurement of interfacial area, interfacial velocity and liquid turbulence in two-phase flow, in: LOECD Meeting on Instrumentation, Santa Barbara, CA, 1997.
[8] C. Suzanne, K. Ellingsen, F. Risso, V. Roig, Local measurement in turbulent bubbly flows, Nucl. Eng. Des. 184 (1998) 319–327.
[9] T. Hibiki, M. Ishii, Experimental study on interfacial area transport in bubbly two-phase flows, Int. J. Heat Mass Transfer 42 (1999) 3019–3035.
[10] G. Kocamustafaogullari, Z. Wang, An experimental study on local interfacial parameters in a horizontal bubbly two-phase flow, Int. J. Multiphase Flow 17 (1991) 553–572.
[11] G. Kocamustafaogullari, W.D. Huang, J. Razi, Measurement and modeling of average void fractions, bubble size and interfacial area, Nucl. Eng. Des. 148 (1994) 437–453.
[12] G. Kocamustafaogullari, W.D. Huang, Internal structure and interfacial velocity development for bubbly two-phase flow, Nucl. Eng. Des. 151 (1994) 79–101.
[13] A. Iskandrani, G. Kojasoy, Local void fraction and velocity field description in horizontal bubbly flow, Nucl. Eng. Des. 204 (2001) 117–128.
[14] G.W. Govier, K. Aziz, The flow of complex mixtures in pipes, Van Nostrand Reihold Company, New York, 1972.
[15] P. Andreussi, A. Paglianti, F.S. Silva, Dispersed bubble flow in horizontal pipes, Chem. Eng. Sci. 54 (1999) 1101–1107.
[16] D. Barnea, A unified model for predicting flow pattern transitions from the whole range of pipe inclination, Int. J. Multiphase Flow 13 (1987) 1–12.
[17] J. Li, M. Kwauk, Particle Fluid Two-phase Flow, Metallurgical Industry Press, Beijing, 1994.
[18] T.L. Holmes, T.W.F. Russell, Horizontal bubble flow, Int. J. Multiphase Flow 2 (1975) 51–66.
[19] D.R.H. Beattie, Flow characteristics of horizontal bubbly pipe flow, Nucl. Eng. Des. 163 (1996) 207–212.
[20] H. Luo, H. Svendsen, Theoretical model for drop and bubble break-up in turbulent dispersions, AIChE J. 42 (1996) 1225–1233.
[21] M.J. Prince, H.W. Blanch, Bubble coalescence and break-up in air sparged bubble columns, AIChE J. 36 (1990) 1485–1499.
[22] A.K. Chesters, G. Hoffman, Bubble coalescence in pure liquids, Appl. Sci. Res. 38 (1982) 353–361.
[23] J.C. Rotta, Turbulente Stromungen, B.G. Teubner, Stuttgart, 1974.

[24] H. Anglart, O. Nylund, CFD application to prediction of void distribution in two-phase bubbly flows in rod bundles, Nucl. Sci. Eng. 163 (1996) 81–98.
[25] R.T. Lahey Jr., D.A. Drew, The analysis of two-phase flow and heat transfer using multidimensional, four field, two-fluid model, Nucl. Eng. Des. 204 (2001) 29–44.
[26] J.B. Joshi, Computational flow modeling and design of bubble column reactors, Chem. Eng. Sci. 55 (21/22) (2001) 5893–5933.
[27] M. Ishii, N. Zuber, Drag coefficient and relative velocity in bubbly, droplet or particulate flows, AIChE J. 25 (1979) 843–855.
[28] I. Zun, The transverse migration of bubbles influenced by walls in vertical bubly flow, Int. J. Multiphase Flow 6 (1980) 583–588.
[29] N.H. Thomas, T.R. Auton, K. Sene, J.C.R. Hunt, Entrapment and transport of bubbles by transient large eddies in turbulent shear flow, in: BHRA International Conference on the Physical Modelling of Multiphase Flow, 1983.
[30] D.A. Drew, S.L. Passman, Theory of Multicomponent Fluids, Springer-Verlag, New York, NY, 1999.
[31] A. Tomiyama, H. Tamai, I. Zun, S. Hosokawa, Transverse migration of single bubbles in simple shear flows, Chem. Eng. Sci. 57 (11) (2002)1849–1858.
[32] M.A. Lopez de Bertodano, Turbulent bubbly two-phase flow in a triangular duct, Ph.D. dissertation, Rensselaer Polytechnic Institute, 1992.
[33] S.P. Antal, R.T. Lahey, J.E. Flaherty, Analysis of phase distribution in fully-developed laminar bubbly two phase flow, Int. J. Multiphase Flow 7 (1991) 635.
[34] Y. Sato, K. Sekoguchi, Liquid velocity distribution in two-phase bubbly flow, Int. J. Multiphase Flow 2 (1975) 79–95.
[35] B.E. Launder, D.B. Spalding, Mathematical Models of Turbulence, Academic Press, London, GB, 1972.
[36] S. Lo, Application of the MUSIG model to bubbly flows, AEAT-1096, AEA Technology, June 1996.